Environ Sci Pollut Res (2017) 24:19435–19443
DOI 10.1007/s11356-017-9566-4

RESEARCH ARTICLE

Degradation of the cyanotoxin microcystin-LR using iron-based photocatalysts under visible light illumination

Changseok Han [1] · Libor Machala [2] · Ivo Medrik [2] · Robert Prucek [2] · Radina P. Kralchevska [2] · Dionysios D. Dionysiou [1]

Received: 26 March 2017 / Accepted: 14 June 2017 / Published online: 4 July 2017

Abstract In this study, a simple and low-cost method to synthesize iron(III) oxide nanopowders in large quantity was successfully developed for the photocatalytic degradation of microcystin-LR (MC-LR). Two visible light-active iron(III) oxide samples (MG-9 calcined at 200 °C for 5 h and MG-11 calcined at 180 °C for 16 h) with a particle size of 5–20 nm were prepared via thermal decomposition of ferrous oxalate dihydrate in air without any other modifications such as doping. The synthesized samples were characterized by X-ray powder diffraction, ^{57}Fe Mössbauer spectroscopy, transmission electron microscopy, Brunauer–Emmett–Teller (BET) specific surface area analysis, and UV–visible diffuse reflectance spectroscopy. The samples exhibited similar phase composition (a mixture of α-Fe_2O_3 and γ-Fe_2O_3), particle size distribution (5–20 nm), particle morphology, and degree of agglomeration, but different specific surface areas (234 $m^2\ g^{-1}$ for MG-9 and 207 $m^2\ g^{-1}$ for MG-11). The results confirmed higher photocatalytic activity of the catalyst with higher specific surface area. The highest photocatalytic activity of the sample to decompose MC-LR was observed at solution pH of 3.0 and catalyst loading of 0.5 g L^{-1} due to large amount of MC-LR adsorption, but a little iron dissolution of 0.0065 wt% was observed. However, no iron leaching was observed at pH 5.8 even though the overall MC-LR removal was slightly lower than at pH 3.0. Thus, the pH 5.8 could be an appropriate operating condition for the catalyst to avoid problems of iron contamination by the catalyst. Moreover, magnetic behavior of γ-Fe_2O_3 gives a possibility for an easy separation of the catalyst particles after their use.

Keywords Microcystin · Mössbauer spectroscopy · Photocatalysis · Iron oxide · Water treatment

Responsible editor: Suresh Pillai

Electronic supplementary material The online version of this article (doi:10.1007/s11356-017-9566-4) contains supplementary material, which is available to authorized users.

✉ Libor Machala
libor.machala@upol.cz

✉ Dionysios D. Dionysiou
dionysios.d.dionysiou@uc.edu

Changseok Han
hanck@mail.uc.edu

Ivo Medrik
ivo.medrik@upol.cz

Robert Prucek
robert.prucek@upol.cz

Radina P. Kralchevska
radina.k@gmail.com

[1] Environmental Engineering and Science Program, Department of Biomedical, Chemical and Environmental Engineering, University of Cincinnati, Cincinnati, OH 45221-0012, USA

[2] Regional Centre of Advanced Technologies and Materials, Departments of Experimental Physics and Physical Chemistry, Faculty of Science, Palacký University, Šlechtitelů 27, 783 71 Olomouc, Czech Republic

Introduction

Iron(III) oxides are known as ubiquitous, chemically stable, cheap, and nontoxic compounds. Their low bandgap energy (~2.2 eV) enables them to collect up to 40% of whole solar spectrum, and they are thus used, among other applications, as photocatalysts in water splitting and water treatment (Mishra and Chun 2015). Many studies reported that α-Fe_2O_3 thin films were successfully applied as semiconducting electrodes for photocatalytic water splitting and hydrogen production (Le

Formal et al., 2010; Sivula et al. 2010; Frydrych et al. 2012; Le Formal et al. 2012; Lopes et al. 2014) and α-Fe_2O_3 nanoparticles or nanotubes effectively decomposed water contaminants, including dyes and 4-chlorophenol under visible light illumination (Khedr et al. 2009; Zhou et al. 2010). The application of α-Fe_2O_3 in disinfection of environment using visible light irradiation was reported as well (Akhavan et al. 2009; Akhavan 2010).

Both α-Fe_2O_3 and γ-Fe_2O_3 have been widely used as photocatalysts to degrade organic and inorganic pollutants in the environment. In particular, α-Fe_2O_3 has been commonly used in many applications due to its higher stability than other iron oxides under ambient conditions (Zhou et al. 2010; Kato and Komatsu 2013). Moreover, it is of great importance to recover used catalysts from water treatment processes for saving resources as well as avoiding additional water filtration causing extra expenses during water treatment. Ferrimagnetic behavior of γ-Fe_2O_3 or Fe_3O_4 gives a possibility to separate the catalysts by applying external magnetic field, e.g., using a permanent magnet. On the other hand, the photocatalytic performance of iron oxides can be limited by low diffusion lengths of holes, poor conductivity, and high rates of electrons (e^-) and hole (h^+) recombination. These difficulties can be significantly overcome by forming nanostructured iron oxides. Therefore, it is required to develop nanostructured magnetic iron oxides for water treatment.

Microcystins (MCs) are the most common toxins produced by harmful cyanobacteria, which can be present in natural water. Microcystin-LR (MC-LR) is mostly found in different water bodies among MCs. Up to now, several approaches of photocatalytic degradation of MC-LR have been investigated mostly based on the application of TiO_2-based nanostructures, such as highly ordered TiO_2 nanotubes (Su et al. 2013), Ag/AgCl/TiO_2 nanotube arrays (Liao et al. 2013), nanostructured nitrogen-doped TiO_2 (Trantis et al. 2012), C-N-codoped TiO_2 films (Liu et al. 2013), Bi-doped TiO_2 (Yang et al. 2011), N-F-codoped TiO_2 films (Pelaez et al. 2010), and sulfur-doped TiO_2 films (Han et al. 2011). Generally, a shift of the bandgap toward visible light was achieved by various kinds of doping of TiO_2. Besides TiO_2-based nanomaterials, AgCl/iron oxide composites were tested for MC-LR photocatalytic degradation (Zhang et al. 2013).

In our study, we used pure Fe_2O_3 nanopowder samples as visible light-active photocatalysts, which have been easily synthesized by thermal decomposition of ferrous oxalate dihydrate without any further processing, for MC-LR degradation under visible light irradiation. It is worth mentioning that such kind of Fe_2O_3 nanopowder consisting of very small nanoparticles (~5 nm) has been also tested in the past as a catalyst for heterogeneous catalysis of decomposition of hydrogen peroxide (Hermanek et al. 2007; Gregor et al. 2010; Hermanek et al. 2010) or degradation of phenol (Prucek et al. 2009).

Material and methods

Ferrous oxalate dihydrate ($FeC_2O_4 \cdot 2H_2O$, Sigma-Aldrich) was used as an iron precursor for thermal synthesis of ferric oxide nanopowders. MC-LR standard (Calbiochem) was purchased, and a MC-LR stock solution of 500 mg L^{-1} was prepared using autoclaved Milli-Q-grade water. For photocatalytic degradation experiments, the stock solution was diluted to 500 μg L^{-1}.

Two iron-containing nanopowder samples were prepared by thermal decomposition of 4 g of ferrous oxalate dihydrate ($FeC_2O_4 \cdot 2H_2O$) in a muffle furnace in air. The calcination at 200 °C for 5 h resulted in sample labeled MG-9, whereas the calcination at 180 °C for 16 h led to sample labeled MG-11.

The as-prepared ferric oxide nanopowders were characterized using X-ray powder diffraction (XRD), ^{57}Fe transmission Mössbauer spectroscopy, transmission electron microscopy (TEM), magnetometry, UV–visible diffuse reflectance spectroscopy (DRS), and Brunauer–Emmett–Teller (BET) physical adsorption technique.

TEM (JEOL JEM-2010) was performed to investigate the detailed morphology of synthesized catalysts at 160 kV with 1.9-Å point-to-point resolution. For TEM analysis, diluted dispersion was fixed on holey carbon film copper grids (from Emsdiasum Company) and then vacuum dried at room temperature.

XRD patterns of the prepared samples were obtained using PANalytical X'Pert PRO diffractometer in Bragg–Brentano geometry with iron-filtered CoKα radiation source, an X'Celerator detector, programmable divergence, and diffracted beam anti-scatter slits. The samples were prepared on a zero-background single crystal silicon slide and measured in continuous mode with a resolution of 0.017° of 2θ. The commercial standards SRM640 for Si and SRM660 for LaB6 from NIST were used to evaluate line positions and instrumental line broadening, respectively. The X'Pert HighScore Plus software (PANalytical, The Netherlands), combined with PDF-4+ and ICSD databases, was used to analyze the obtained patterns.

A transmission MS96 Mössbauer spectrometer (Pechoušek et al. 2012) with a ^{57}Co(Rh) source of γ-rays was employed for the zero-field Mössbauer experiment at 300 K. The recorded spectra were fitted by the Lorentzian line shapes with the MossWinn program (Klencsár et al. 1996) based on the least-square method. The values of isomer shift were referred to α-Fe foil samples at room temperature.

UV–vis absorption spectra of the iron oxide nanoparticle dispersions were acquired in a quartz cuvette using a Specord S 600 spectrophotometer (Analytic Jena AG, Germany) in a range from 200 to 800 nm.

Surface areas of the prepared iron oxide nanopowders were characterized with nitrogen adsorption–desorption measurements. Adsorption–desorption isotherms were measured at

temperature of liquid nitrogen (77.4 K). Experimental points acquired by the statistic volumetric technique were obtained by a Thermo Finnigan Sorptomatic 1990 analyzer. Before the measurement, the surface of the nanopowders was degassed at room temperature for at least 20 h. BET surface areas were determined with the multipoint BET(3) model. The analysis was performed using an ADP (Advanced Data Processing) 4.0 software package (CE Instruments). Samples were measured with identical settings of number adsorption and desorption points under the same analysis conditions.

Magnetic data were obtained with a Quantum Design Physical Property Measurement System (PPMS DynaCool system, Quantum Design) with the VSM option. Diamagnetism of samples and a signal of the sample holder were collected. The hysteresis loop was recorded at 300 K with external magnetic fields in a range of −5 to +5 T.

Concentrations of metal ions within leaching tests were measured by an atomic absorption spectroscopy (AAS) using a ContrAA 300 flame ionizer (Analytik Jena AG, Germany) with a high-resolution Echelle double monochromator (spectral bandwidth of 2 pm at 200 nm) and a continuum radiation source (xenon lamp). The absorption line used for the analyses of Fe content was 248.3270 nm. Calibration standards of Fe for performing AAS were of TraceCERT (1 g L^{-1}) type, purchased from Fluka. Solutions were prepared using deionized water (18 MΩ cm^{-1}, Millipore).

For the evaluation of the photocatalytic activity of the prepared iron oxide nanopowders under visible light irradiation, a reactor (glass petri dish, dia. 60 mm) was used. For visible light irradiation (Zhao et al. 2013), two Cole-Parmer 15-W fluorescent lamps were employed with an actual light intensity of 3.99×10^{-4} W cm^{-2} and a UV420 Opticology filter was employed to eliminate UV component from the lamp spectra. The spectra of visible light are available in Additional file 1: Fig. S1 in a previous study (Han et al. 2014). A reactor containing 10 mL total volume of the solution was used to evaluate the visible light-induced photocatalytic activity of the two catalysts for MC-LR degradation.

The initial MC-LR concentration and catalyst loading were 500 μg L^{-1} and 0.5 g L^{-1}, respectively. To investigate the effects of catalyst loading on the MC-LR degradation, three catalyst loadings (0.25, 0.5, and 1.0 g L^{-1}) were tested. To explore the effects of the initial pH of solution on the decomposition of MC-LR, experiments were performed at four different pH values (3.0, 5.8, 7.0, and 10.0). To study MC-LR degradation under visible light, the reactor was placed in the dark for the initial 3 h to reach adsorption equilibrium since the initial MC-LR concentration was very low, and then exposed to visible light for 5 h. Aliquot samples of 200 μL were taken at reaction times of 0, 1, and 3 h under dark condition and 1, 2, 3, and 5 h under visible light illumination. A high-performance liquid chromatograph (HPLC, Agilent Series 110) was used with the previously reported analytical method to measure the concentration of MC-LR in the samples. A Discovery HS C18 column (150 mm × 2.1 mm, 5-μm particle size, Supelco, Bellefonte, PA, USA) was equipped in HPLC. The flow rate of mobile phase was 0.2 mL min^{-1}, the sample injection volume was 20 μL, and the column temperature was 45 °C. For safety issue, all experiments were performed in an advanced SterilchemGARD III Class II biological safety cabinet (Baker Company, Sanford, ME) (Pelaez et al. 2009; Han et al. 2011). All experiments were performed three times to confirm the reproducibility.

In order to confirm the stability of the Fe_2O_3 catalysts in water under lower pH values, leaching tests were performed. Catalyst concentrations equal to 0.5 g L^{-1} and pH values equal to 3.0 and 5.8. The 50 mL of catalyst solution was shaken on a conventional multi-rotator shaker (Multi RS-60, Biosan) in 60-mL vials. Aliquot samples of 5 mL were taken at reaction times of 3, 8, and 24 h and subsequently three times filtered through 0.2-μm syringe filters before Fe content in the filtered solution was analyzed by AAS.

Results and discussions

Synthesis and characterization of ferric oxide nanopowders

XRD patterns of both MG-9 and MG-11 samples (Fig. 1) show the presence of two crystalline ferric oxide phases: γ-Fe_2O_3 and α-Fe_2O_3. Relative weight contents, mean X-ray coherence lengths, and cell parameters are summarized in Table 1. In addition to crystalline γ-Fe_2O_3 and α-Fe_2O_3 with the small X-ray coherence lengths 8 and 6 nm, respectively, the XRD patterns indicate the presence of amorphous phase as well.

Room-temperature Mössbauer spectra of both samples (Fig. 2) were fitted by doublets corresponding to (super) paramagnetic Fe(III) in an octahedral coordination and distributions of hyperfine magnetic fields originating from particles with sizes, which are slightly above the limit for superparamagnetism. The hyperfine parameters are summarized in Table 2. Maghemite and hematite particles of ferric oxide contribute to both superparamagnetic doublet and sextet components in case of both studied samples. This overlap is well demonstrated by the value of quadrupole shift of −0.16 mm s^{-1} for the sextet of sample MG-9, which lies between the value of −0.21 mm s^{-1} for hematite and approximately zero for maghemite. Therefore, a quantification of the phase composition was not possible to perform like in the case of XRD analysis.

TEM images of MG-9 and MG-11 samples (Fig. 3) show strongly agglomerated nanoparticles with size in the range from 5 to 20 nm. Specific surface areas (BET) of MG-9 and

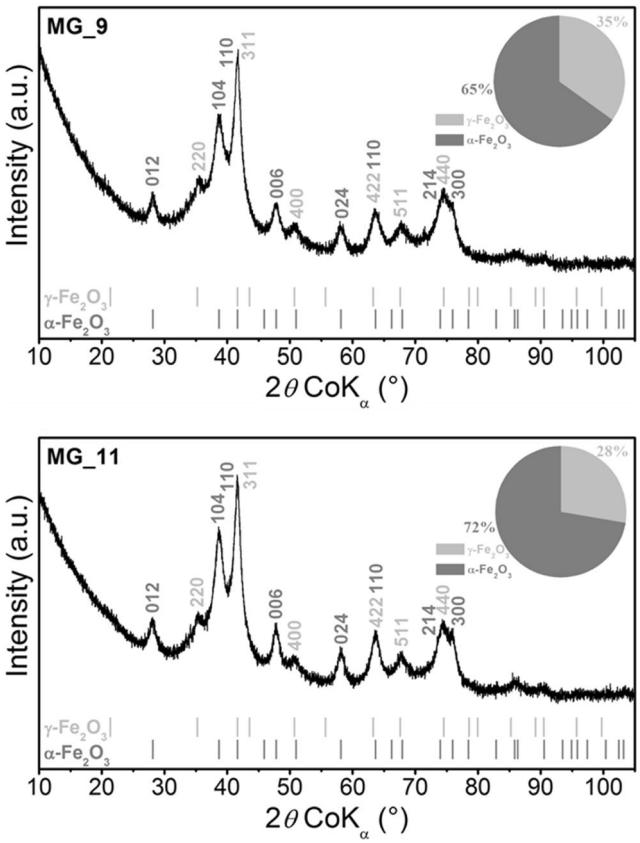

Fig. 1 X-ray diffraction patterns of MG-9 (*top*) and MG-11 (*bottom*) samples. The positions of Bragg reflection of each identified phase are shown under the pattern. The quantification of identified phases is presented on the *right side*

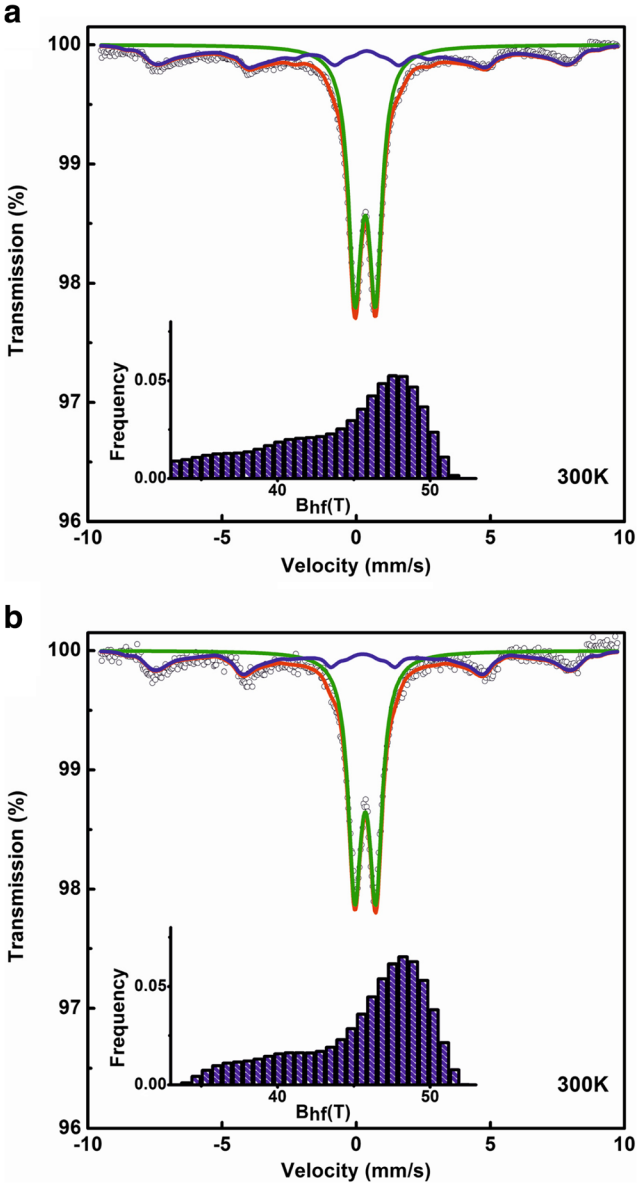

Fig. 2 Room-temperature Mössbauer spectra of MG-9 (**a**) and MG-11 (**b**) samples

MG-11 samples were determined as 234 and 207 $m^2\ g^{-1}$, respectively. Moreover, the light absorption of MG-9 and MG-11 was measured with DRS. Both MG-9 and MG-11 effectively absorbed a broad range of UV–visible light from 200 to 800 nm, and their light absorption properties were pretty much the same (Additional file 1: Fig. SI1). Zero point charges were measured for the both MG-9 and MG-11 samples. The results are summarized in Additional file 1: Table SI1.

Magnetic properties of sample MG-9 were investigated by measuring of hysteresis loop at room temperature (Fig. 4). The "S" shape of the curve is typical for superparamagnetic behavior of nanoparticles. There is no saturation of the curve at the highest magnetic fields, which is due to the presence of

Table 1 The phases identified in the XRD patterns with specified parameters derived by Rietveld refinement

Sample	Phase	JCPDS code	Phase content (wt%)	MCL (nm)	Cell parameter (nm)
MG_9	Maghemite γ-Fe_2O_3	04-008-8146	35	8	0.8341
	Hematite α-Fe_2O_3	01-089-0596	65	6	0.5039
					1.3696
MG_11	Maghemite γ-Fe_2O_3	04-008-8146	28	8	0.8343
	Hematite α-Fe_2O_3	01-089-0596	72	6	0.5036
					1.3709

JCPDS code ID code of identified phase in PDF-4+ database, *MCL* mean X-ray coherence length

Table 2 Hyperfine parameters and relative spectral areas calculated from room-temperature spectra of samples MG-9 and MG-11

Sample	Component	δ_{Fe} (mm s^{-1})	ΔE_Q (ε_Q) (mm s^{-1})	B_{av} (*T*)	RA (%)
MG-9	Doublet	0.34	0.77	–	63.2
	Sextet (distribution)	0.31	−0.16	48	36.8
MG-11	Doublet	0.34	0.78	–	67.6
	Sextet (distribution)	0.25	0	48	32.4

δ_{Fe} isomer shift related to metallic iron, ΔE_Q quadrupole splitting for doublets, ε_q quadrupole shift for sextets, B_{av} most probable hyperfine field, *RA* relative spectral area

hematite in the sample. The maximum measured magnetization reached the value of 16.2 emu g^{-1}, which is enough for attracting the nanopowder iron oxides to a conventional permanent magnet. Remanent magnetization as well as coercivity is almost zero. Similar magnetic behavior for sample MG-11 at room temperature is expected. In order to confirm possibility of magnetic separation of the samples in water, an ordinary permanent magnet was placed into the vials with MG-9 and MG-11 samples dispersed in water. Nanoparticles of both samples were separated in the proximity of the magnet during approx. 2 min. The experiment is illustrated by the photos in Fig. 5.

Degradation of MC-LR using the ferric oxide nanopowders

MG-9 ferric oxide sample showed higher photocatalytic activity to decompose MC-LR in water under visible light irradiation in comparison with MG-11 sample at the given conditions (i.e., pH 5.8, 500 μg L^{-1} of initial concentration of MC-LR and 0.5 g L^{-1} of the catalyst loading). As seen in Fig. 6, MG-9 and MG-11 adsorbed about 26 and 8% MC-LR, respectively, under the dark condition for 3 h. After 5 h of visible light illumination, total removal of MC-LR was 86% for MG-9 and 40% MC-LR for MG-11. Based on the results, 60 and 32% MC-LR was decomposed by visible light-induced MG-9 and MG-11 photocatalysis, respectively. The phase composition as well as morphology and degree of agglomeration of nanoparticles is almost the same for both tested samples as it is documented by practically the same shapes of the BET isotherms (Additional file 1: Fig. SI2). Also, as mentioned in "Synthesis and characterization of ferric oxide nanopowders" section, the light absorption property of both samples was similar in a range of wavelength from 200 to 800 nm. The nanopowder photocatalysts differ in specific surface area (234 vs. 207 m^2 g^{-1}) that evidently contributed to the difference in the extent of MC-LR removal. The MC-LR removal per unit surface area was 3.72 μg m^{-2} for MG-9 and 2.03 μg m^{-2} for MG-11.

Further, different loadings of MG-9 sample were tested in the decomposition of MC-LR under visible light irradiation (Fig. 7) since this sample demonstrated higher photocatalytic activity than MG-11 sample. The photocatalytic degradation of MC-LR with MG-9 under visible light followed pseudo *first-order* kinetics with the observed rate constant of 0.0359, 0.3289, and 0.0518 h^{-1} for 0.2, 0.5, and 1.0 g L^{-1} of MG-9, respectively (see Additional file 1: Fig. SI3). At 0.5 g L^{-1} of MG-9 loading, the highest MC-LR removal was observed. At lower loading of catalysts (<0.5 g L^{-1}), lower number of active sites of the catalysts may be involved to decompose MC-LR. Moreover, the degradation of MC-LR decreased at higher loading (>0.5 g L^{-1}) due to particle agglomeration and the increase of turbidity of solution, associated with light penetration. Therefore, the optimal catalyst loading (0.5 g L^{-1}) was used to investigate the effect of initial pH of solution on the degradation of MC-LR under visible light irradiation.

To investigate the effect of initial pH of solution on the degradation of MC-LR under visible light illumination, the pH of solution was adjusted using nitric acid or 10% sodium hydroxide solution. Higher concentration of MC-LR (750 μg L^{-1}) was used for appropriate HPLC analysis. At pH 3, MG-9 showed the highest removal of MC-LR along with the highest adsorption of MC-LR due to high electrostatic

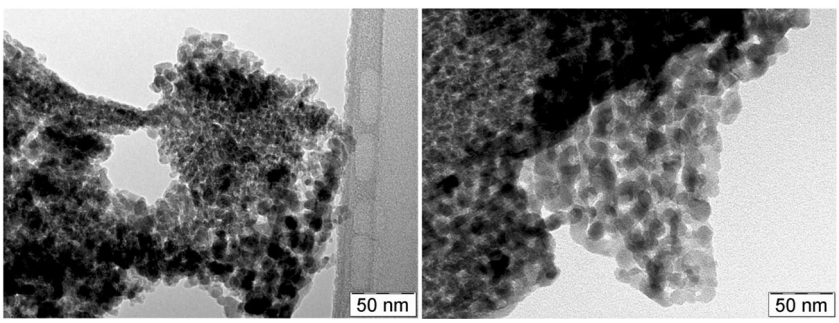

Fig. 3 TEM images of MG-9 (*left*) and MG-11 (*right*) samples

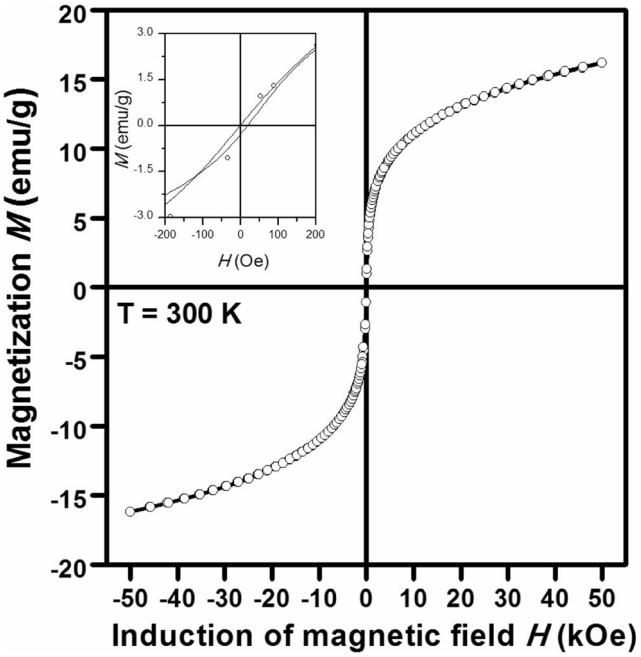

Fig. 4 Hysteresis loop for sample MG-9 at room temperature. The *inset* shows that remanent magnetization as well as coercivity is almost zero

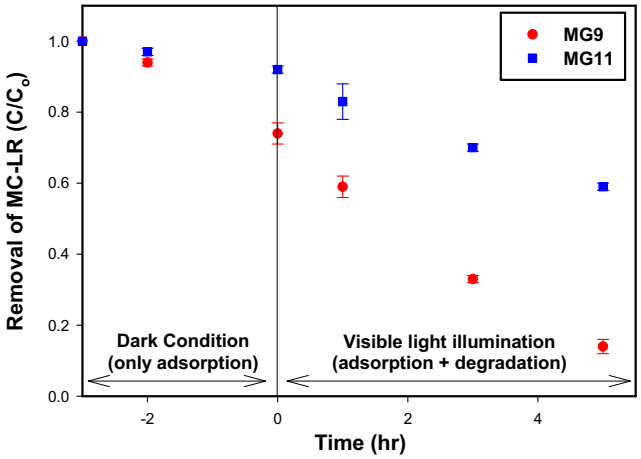

Fig. 6 The removal of MC-LR for MG-9 and MG-11 samples at pH 5.8 with a 500 μg L^{-1} of MC-LR and the catalyst loading of 0.5 g L^{-1}

attraction because MC-LR is negatively charged but iron oxides are positively charged (Mustafa et al. 2004; Gao and Chorover 2010; Pelaez et al. 2011). After 5 h of visible light irradiation, 70.5% MC-LR was removed (Fig. 8). The total removal of MC-LR was inversely proportional to the initial pH of solutions (Fig. 8b). These results may also be caused by Fenton reaction due to dissolution of iron at low pH (i.e., 3.0). Fe_2O_3 produces pairs of electrons (e^-) and holes (h^+) via light absorption (Eq. (1)) (Kiwi and Grätzel 1987; Shelton et al. 2016) and hydroxyl radical (·OH) and superoxide anions ($O_2{\cdot}^-$) form according to Eqs. (2) and (3). Also, hydrogen peroxide (H_2O_2) could be produced according to Eqs. (4), (5), (6), and (7) (Zhao et al. 2014; Khan et al. 2016). Formed H_2O_2 reacts with dissolved iron (Eq. (8)) via Fenton reaction (Ruppert et al. 1993; Winterbourn 1995), which improves the efficiency of visible light-induced Fe_2O_3 photocatalysis to decompose MC-LR at pH 3.

$$Fe_2O_3 + h\nu \rightarrow h^+ + e^- \quad (1)$$

$$h^+ + H_2O \rightarrow {}^{\bullet}OH + H^+ \quad (2)$$

$$e^- + O_2 \rightarrow O_2^{\bullet-} \quad (3)$$

$$e^- + O_2^{\bullet-} + 2H^+ \rightarrow H_2O_2 \quad (4)$$

$$O_2^{\bullet-} + O_2^{\bullet-} + 2H^+ \rightarrow H_2O_2 + O_2 \quad (5)$$

$$O_2^{-\bullet} + H^+ \rightarrow HO_2^{\bullet} \quad (6)$$

$$2HO_2^{\bullet} + 2H^+ \rightarrow 2H_2O_2 + O_2 \quad (7)$$

$$Fe^{2+} + H_2O_2 \rightarrow Fe^{3+}OH^- + {}^{\bullet}OH \quad (8)$$

In order to confirm a stability of the Fe_2O_3 catalysts in water under acidic solution conditions (i.e., pH 5.8 and pH 3.0), leaching tests were performed since iron oxides (i.e., lepidocrocite, ferrihydrite, hematite, goethite, ferrihydrite, and "soil-Fe") show the minimal solubility at pH 7–8 (experimental details are mentioned in the "Material and methods" section) (Cornell and Schwertmann 2003). The results showed no leaching of Fe_2O_3 at pH = 5.8 even after 24 h of the experiment within the detection limit of the method (0.2 mg L^{-1} of Fe, which was determined as the end of the calibration curve). Addition of Fe_2O_3 nanopowder to water with pH = 3.0 led to dissolution of 0.065 wt% of Fe_2O_3 after 8 h of the experiment, and this value remained almost the same after the subsequent 16 h. Iron (Fe^{2+}) dissolved at

Fig. 5 Magnetic separation of the catalysts by using of a permanent magnet. *Left*: the samples before application of the magnet; *right*: the most of nanoparticles are attracted to the magnet during 2 min

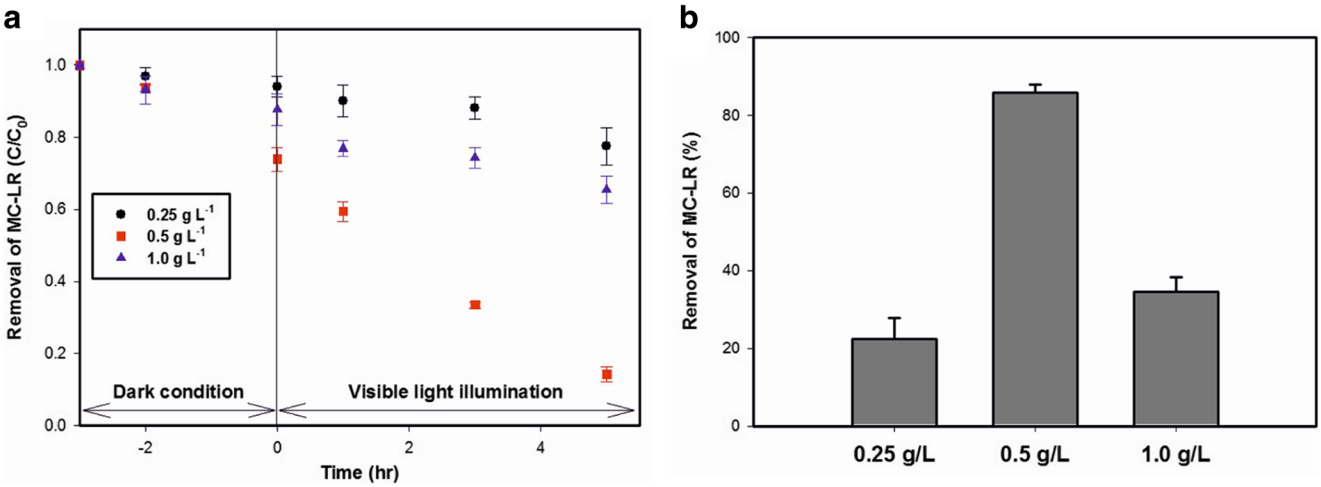

Fig. 7 **a** The effect of catalyst loadings for MG-9 on the removal of MC-LR at pH 5.8 with 500 μg L^{-1} of MC-LR. **b** Total removal of MC-LR with different loadings of MG-9 after 5 h of visible light irradiation at pH 5.8 with 500 μg L^{-1} of MC-LR

pH 3.0 reacted with formed H_2O_2 (Eq. (8)) during visible light-induced Fe_2O_3 photocatalysis, resulting in the enhanced removal of MC-LR. However, the observed rate constant of pseudo *first-order* kinetics for the photocatalytic degradation of MC-LR at different pH values was 0.0648, 0.0811, 0.0325, and 0.0123 h^{-1} at pH 3.0, 5.8, 7.0, and 10.0, respectively (see Additional file 1: Fig. SI4). It seems that the photocatalytic degradation of MC-LR at pH 5.8 was higher than at pH 3.0, but the actual removal of MC-LR at pH 3.0 is still high. At that pH value, MC-LR of ~35% was adsorbed on MG-9 and it significantly contributed to the overall MC-LR removal. Although the highest removal of MC-LR was obtained at pH 3.0, pH 5.8 could be an appropriate operating condition for the catalyst to avoid any iron contamination problems (Kohgo et al. 2008).

Concerning the issue of using of a mixture of maghemite and hematite as photocatalyst, it is expected that the mixture can lead to the higher photocatalytic activity than maghemite or hematite alone. The bandgaps for maghemite and hematite are almost the same (2.02 eV), but they have different positions. Hematite has a conduction band level at −0.62 V and a valence band level at +1.40 V; maghemite has the two band levels at −0.08 and +1.94 V, respectively (Leland and Bard 1987). In the mixture, the excited electrons at the conduction band of hematite would transfer to the conduction band of maghemite easily. This leads to an effective electron separation and transformation within the iron oxides.

Conclusion

Pure α-Fe_2O_3/γ-Fe_2O_3 nanopowders were proved to be promising as photocatalysts in the removal of the cyanotoxin MC-LR. Higher specific surface area of the photocatalysts led to a

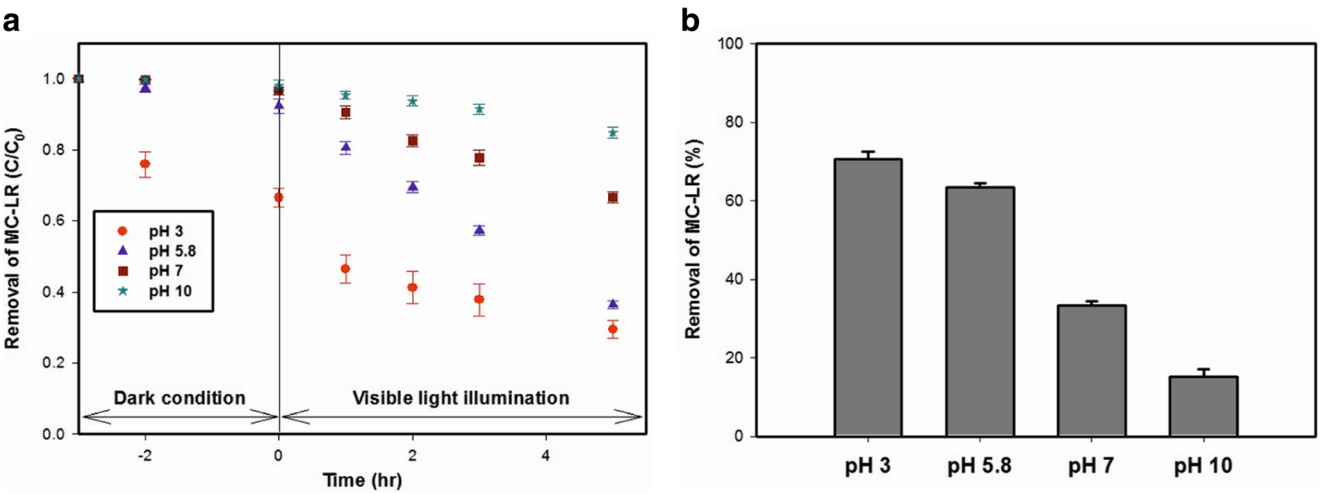

Fig. 8 **a** The effect of initial pH for MG-9 on the removal of MC-LR at 750 μg L^{-1} of MC-LR with 0.5 g L^{-1} of MG-9. **b** The effect of initial pH for MG-9 on the removal of MC-LR after 5 h of visible light illumination at 750 μg L^{-1} of MC-LR with 0.5 g L^{-1} of MG-9

significant increase of the degradation efficiency. The catalyst loading of 0.5 g L^{-1} was shown to be optimal; lower or higher loadings resulted in a decrease of the efficiency under the experimental conditions in this study. Solution pH proved to be an important parameter for Fe_2O_3 photocatalysis for the removal of MC-LR due to iron dissolution. The dissolved iron could react with formed H_2O_2 during the photocatalysis process, improving the efficiency of the photocatalysis process via Fenton reaction. Even though the highest photocatalytic degradation of MC-LR was achieved at pH 3, solution pH needs to be carefully controlled to avoid iron contamination problems by iron dissolution. These investigations could be continued by a test of other Fe_2O_3 nanoparticulate systems, like amorphous Fe_2O_3 or beta-Fe_2O_3, to improve the efficiency of iron oxide photocatalysis for the degradation of contaminants in water. Also, in future, it would be interesting to confirm whether the Fe_2O_3 catalysts could be regenerated and reused for more than one photocatalytic test/cycle, e.g., by employing of magnetic separation.

Acknowledgements The authors gratefully acknowledge the financial support provided by the project LO1305 of the Ministry of Education, Youth and Sports of the Czech Republic and by Operational Program Education for Competitiveness—European Social Fund (projects CZ.1.07/2.3.00/30.0004 and CZ.1.07/2.3.00/20.0058). The authors thank Petr Novak, Michal Krizek, Klara Cepe, Ondrej Malina, and Josef Kaslik (all at Palacký University in Olomouc, Czech Republic) for the characterization of nanopowders. D.D. Dionysiou also acknowledges support from the University of Cincinnati through a UNESCO cochair professor position on "Water Access and Sustainability."

References

Akhavan O (2010) Thickness dependent activity of nanostructured TiO_2/α-Fe_2O_3 photocatalyst thin films. Appl Surf Sci 257:1724–1728. doi:10.1016/j.apsusc.2010.09.005

Akhavan O, Azimirad R (2009) Photocatalytic property of Fe_2O_3 nanograin chains coated by TiO_2 nanolayer in visible light irradiation. Appl Catal A Gen 369:77–82. doi:10.1016/j.apcata.2009.09.001

Cornell RM, Schwertmann U (2003) The iron oxides: structure, properties, reactions, occurrences and uses, Second edn. Wiley-Vch Verlag GmbH & Co., Weinheim

Frydrych J, Machala L, Tucek J, Siskova K, Filip J, Pechousek J, Safarova K, Vondracek M, Seo JH, Schneeweiss O, Greatzel M, Sivula K, Zboril R (2012) Facile fabrication of tin-doped hematite photoelectrodes—effect of doping on magnetic properties and performance for light-induced water splitting. J Mater Chem 22:23232–23239. doi:10.1039/C2JM34639G

Gao X, Chorover J (2010) Adsorption of sodium dodecyl sulfate (SDS) at ZnSe and α-Fe_2O_3 surfaces: combining infrared spectroscopy and batch uptake studies. J Colloid Interface Sci 348:167–176. doi:10.1016/j.jcis.2010.04.011

Gregor C, Hermanek M, Jancik D, Pechousek J, Filip J, Hrbac J, Zboril R (2010) The effect of surface area and crystal structure on the catalytic efficiency of iron(III) oxide nanoparticles in hydrogen peroxide decomposition. Eur J Inorg Chem 2010:2343–2351. doi:10.1002/ejic.200901066

Han C, Pelaez M, Likodimos V, Kontos AG, Falaras P, O'Shea K, Dionysiou DD (2011) Innovative visible light-activated sulfur doped TiO_2 films for water treatment. Appl Catal B 107:77–87. doi:10.1016/j.apcatb.2011.06.039

Han C, Likodimos V, Khan JA, Nadagouda MN, Andersen J, Falaras P, Rosales-Lombardi P, Dionysiou DD (2014) UV–visible light-activated Ag-decorated, monodisperse TiO_2 aggregates for treatment of the pharmaceutical oxytetracycline. Environ Sci Pollut Res 21:11781–11793. doi:10.1007/s11356-013-2233-5

Hermanek M, Zboril R, Medrik I, Pechousek J, Gregor C (2007) Catalytic efficiency of iron(III) oxides in decomposition of hydrogen peroxide: competition between the surface area and crystallinity of nanoparticles. J Am Chem Soc 129:10929–10936. doi:10.1021/ja072918x

Hermanek M, Hermankova P, Pechousek J (2010) Quasi-isothermal decomposition: a way to nanocrystalline mesoporous-like Fe_2O_3 catalyst for rapid heterogeneous decomposition of hydrogen peroxide. J Mater Chem 20:3709–3715. doi:10.1039/C000632G

Kato R, Komatsu T (2013) Structure and photocatalytic activity of iron oxide nanotubes prepared from ferritin. J Inorg Organomet Polym 23:167–171. doi:10.1007/s10904-012-9725-5

Khan S, Han C, Khan HM, Boccelli DL, Nadagouda MN, Dionysiou DD (2016) Efficient degradation of lindane by visible and simulated solar light-assisted S-TiO_2/peroxymonosulfate process: kinetics and mechanistic investigations. J Mol Catal A. doi:10.1016/j.molcata.2016.11.035

Khedr MH, Abdel Halin KS, Soliman NK (2009) Synthesis and photocatalytic activity of nano-sized iron oxides. Meter Lett 63:598–601. doi:10.1016/j.matlet.2008.11.050

Kiwi J, Grätzel M (1987) Light-induced hydrogen formation and photo-uptake of oxygen in colloidal suspensions of α-Fe_2O_3. J Chem Soc Faraday Trans 83:1101–1108. doi:10.1039/F19878301101

Klencsár Z, Kuzmann E, Vértes A (1996) User-friendly software for Mössbauer spectrum analysis. J Radioanal Nucl Chem 210:105–118. doi:10.1007/BF02055410

Kohgo Y, Ikuta K, Ohtake T, Torimoto Y, Kato J (2008) Body iron metabolism and pathophysiology of iron overload. Int J Hematol 88:7–15. doi:10.1007/s12185-008-0120-5

Le Formal F, Gratzel M, Sivula M (2010) Controlling photoactivity in ultrathin hematite films for solar water-splitting. Adv Funct Mater 20:1099–1107. doi:10.1002/adfm.200902060

Le Formal F, Sivula K, Grätzel M (2012) The transient photocurrent and photovoltage behavior of a hematite photoanode under working conditions and the influence of surface treatments. J Phys Chem C 116:26707–26720. doi:10.1021/jp308591k

Leland JK, Bard AJ (1987) Photochemistry of colloidal semiconducting iron oxide polymorphs. J Phys Chem 91(19):5076–5083. doi:10.1021/j100303a039

Liao W, Zhang Y, Zhang M, Murugananthan M, Yoshihara S (2013) Photoelectrocatalytic degradation of microcystin-LR using Ag/AgCl/TiO_2 nanotube arrays electrode under visible light irradiation. Chem Eng J 231:455–463. doi:10.1016/j.cej.2013.07.054

Liu G, Han C, Pelaez M, Zhu D, Liao S, Likodimos V, Kontos AG, Falaras P, Dionysiou DD (2013) Enhanced visible light photocatalytic activity of C-N-codoped TiO_2 films for the degradation of microcystin-LR. J Mol Catal A 372:58–65. doi:10.1016/j.molcata.2013.02.006

Lopes T, Andrade L, Le Formal F, Gratzel M, Sivula K, Mendes A (2014) Hematite photoelectrodes for water splitting: evaluation of the role of film thickness by impedance spectroscopy. Phys Chem Chem Phys 16:16515–16523. doi:10.1039/c3cp55473b

Mishra M, Chun D-M (2015) α-Fe_2O_3 as a photocatalytic material: a review. Appl Catal A: General 498:126–141. doi:10.1016/j.apcata.2015.03.023

Mustafa S, Tasleem S, Naeem A (2004) Surface charge properties of Fe_2O_3 in aqueous and alcoholic mixed solvents. J Colloid Interface Sci 275:523–529. doi:10.1016/j.jcis.2004.02.089

Pechoušek J, Jančík D, Frydrych J, Navařík J, Novák P (2012) Setup of Mössbauer spectrometers at RCPTM. AIP Conf Proc 1489:186–193. doi:10.1063/1.4759489

Pelaez M, de la Cruz AA, Stathatos E, Falaras P, Dionysiou DD (2009) Visible light-activated N-F-codoped TiO_2 nanoparticles for the photocatalytic degradation of microcystin-LR in water. Catal Today 144:19–25. doi:10.1016/j.cattod.2008.12.022

Pelaez M, Falaras P, Likodimos V, Kontos AG, de la Cruz AA, O'Shea K, Dionysiou DD (2010) Synthesis, structural characterization and evaluation of sol–gel-based NF-TiO_2 films with visible light-photoactivation for the removal of microcystin-LR. Appl Catal B 99:378–387. doi:10.1016/j.apcatb.2010.06.017

Pelaez M, de la Cruz AA, O'Shea K, Falaras P, Dionysiou DD (2011) Effects of water parameters on the degradation of microcystin-LR under visible light-activated TiO_2 photocatalyst. Water Res 45:3787–3796. doi:10.1016/j.watres.2011.04.036

Prucek R, Hermanek M, Zboril R (2009) An effect of iron(III) oxides crystallinity on their catalytic efficiency and applicability in phenol degradation—a competition between homogeneous and heterogeneous catalysis. Appl Catal A 366:325–332. doi:10.1016/j.apcata.2009.07.019

Ruppert G, Bauer R, Heisler G (1993) The photo-Fenton reaction—an effective photochemical wastewater treatment process. J Photochem Photobiol A 73:75–78. doi:10.1016/1010-6030(93)80035-8

Shelton TL, Harvey N, Wang J, Osterloh FE (2016) Photochemistry of hematite photoanodes under zero applied bias. Appl Catal A 521:168–173. doi:10.1016/j.apcata.2015.11.041

Sivula K, Zboril R, Le Formal F, Robert R, Weidenkaff A, Tucek J, Frydrych J, Grätzel M (2010) Photoelectrochemical water splitting with mesoporous hematite prepared by a solution-based colloidal approach. J Am Chem Soc 132:7436–7444. doi:10.1021/ja101564f

Su Y, Deng Y, Du Y (2013) Alternative pathways for photocatalytic degradation of microcystin-LR revealed by TiO_2 nanotubes. J Mol Catal A 373:18–24. doi:10.1016/j.molcata.2013.02.031

Triantis TM, Fotiou T, Kaloudis T, Kontos AG, Falaras P, Dionysiou DD, Pelaez M, Hiskia A (2012) Photocatalytic degradation and mineralization of microcystin-LR under UV-A, solar and visible light using nanostructured nitrogen doped TiO_2. J Hazard Mater 211-212:196–202. doi:10.1016/j.jhazmat.2011.11.042

Winterbourn CC (1995) Toxicity of iron and hydrogen peroxide: the Fenton reaction. Toxicol Lett 82-83:969–974. doi:10.1016/0378-4274(95)03532-X

Yang J, Chen DX, Deng AP, Huang YP, Chen CC (2011) Visible-light-driven photocatalytic degradation of microcystin-LR by Bi-doped TiO_2. Res Chem Intermed 37:47–60. doi:10.1007/s11164-010-0224-4

Zhang Y, Zhang Y, Tan J (2013) Novel magnetically separable AgCl/iron oxide composites with enhanced photocatalytic activity driven by visible light. J Alloys Comp 574:383–390. doi:10.1016/j.jallcom.2013.05.179

Zhao C, Pelaez M, Duan X, Deng H, O'Shea K, Fatta-Kassinos D, Dionysiou DD (2013) Role of pH on photolytic and photocatalytic degradation of antibiotic oxytetracycline in aqueous solution under visible/solar light: kinetics and mechanism studies. Appl Catal B 134-135:83–92. doi:10.1016/j.apcatb.2013.01.003

Zhao C, Pelaez M, Dionysiou DD, Pillai SC, Byrne JA, O'Shea KE (2014) UV and visible light activated TiO_2 photocatalysis of 6-hydroxymethyl uracil, a model compound for the potent cyanotoxin cylindrospermopsin. Catal Today 224:70–76. doi:10.1016/j.cattod.2013.09.042

Zhou X, Yang H, Wang C, Mao X, Wang Y, Yang Y, Liu G (2010) Visible light induced photocatalytic degradation of rhodamine B on one-dimensional iron oxide particles. J Phys Chem C 114:17051–17061. doi:10.1021/jp103816e